

Implementation of a double-path multi-mode interferometer using spinor BEC

Pengju Tang,¹ Xiangyu Dong,¹ Wenjun Zhang,¹ Yunhong Li,² Xuzong Chen,¹ and Xiaoji Zhou^{1,3,*}

¹*State Key Laboratory of Advanced Optical Communication System and Network,
Department of Electronics, Peking University, Beijing 100871, China*

²*School of Electronics and Information, Xi'an Polytechnic University, Xi'an 710048, China*

³*Collaborative Innovation Center of Extreme Optics,
Shanxi University, Taiyuan, Shanxi 030006, China*

(Dated: September 1, 2022)

We realize a double-path multi-mode matter wave interferometer with spinor Bose-Einstein condensate (BEC) and observe clear spatial interference fringes as well as a periodic change of the visibility in the time domain, which we refer to as the time domain interference and is different from the traditional double-path interferometer. By changing the relative phase of the two paths, we find that the spatial fringes first lose coherence and recover. As the number of modes increases, the time domain interference signal with the narrower peaks is observed, which is beneficial to the improvement of the resolution of the phase measurement. We also investigated the influence of initial phase configuration and phase evolution rate between different modes in the two paths. With enhanced resolution, the sensitivity of interferometric measurements of physical observables can also be improved by properly assigning measurable quantities to the relative phase between two paths.

PACS numbers: 03.75.Dg, 03.75.Mn, 03.75.-b, 03.65.Ta

I. INTRODUCTION

Matter wave interferometers have brought us exciting opportunities of implementing high-precision measurements in both science and technology, including quantum information, quantum simulation and gravity measurements[1–4], as well as insight into fundamental issues of quantum physics such as internal properties of atoms, many-body phenomena and the interplay between general relativity and quantum mechanics[5–10]. Many researches have been carried out which focused on achieving a high performance of interferometers[11–13]. In particular, the sensitivity, one of the important indicators of the ability of an interferometer, received much attention. Most of previous researches implemented a double-path configuration as the model of studying the sensitivity of measurements and gave the limits of the sensitivity, shot-noise limit and sub-shot-noise limit[14, 15]. However, in experiment it needs to take a lot of effort to reduce the noise to reach the noise limit.

Therefore, to suppress the noises from experimental systems and improve the resolution (and thus the sensitivity) of the signal becomes a major concern. Noise-resilient parallel multicomponent interferometer[16] was implemented and effectively enhanced the robustness of measurements of phases. Also, some proposed to increase the number of paths M so as to sharpen the peaks in the interference fringes[17–21]. It has been demonstrated by experiments of internal-state multipath interferometers using spinor BEC that, as long as the scaling of slope with M exceeds \sqrt{M} scaling of the shot noise, the sensitivity improves with the number of paths[22, 23].

Further, some people seek to implement double-path multi-mode interferometers[24–27] to improve the resolution, which means there're several components (e.g., different spin orientations of a BEC) in each path instead of a single component in traditional interferometers. Their advantage is that additional modes would not boost the shot noise, as long as the modes don't interact with each other[28, 29]. The modes of a multi-mode interferometer could be chosen as either spin states or non-interacting external states. Especially, double-path two-mode interferometers[30] (using spin states as the modes) have shown that the modes in each path exhibit good controllability of phase under magnetic fields. These experiments, together with one of our previous work[31] which implemented a full-spin Stern-Gerlach interferometer, demonstrated that the feasibility of using internal states to implement multi-mode interferometers.

In this work, we propose and realize a method to implement double-path multi-mode interferometer with spinor BEC as internal modes to investigate the resolution by using the techniques of Majorana transition and radio-frequency (RF) coupling. In gradient magnetic field, the phase evolution rate of the two paths has a tunable fixed difference, which allow us to control the relative phase between modes by tuning the phase evolution time. Therefore, unlike traditional double-path interferometers, our interferometer not only shows spatial interference fringes, but also exhibits a periodic dependence of visibility on the phase evolution time, which we refer to as the time domain interference. This so-called time domain fringe could be used to measure the phase-shift and the corresponding observables. The sharpness of the time domain fringe improves as the number of the modes increases, which allows us to enhance the resolution of the interferometer. Our experiments demonstrate the existence of the time domain fringes and its dependence on number

* xjzhou@pku.edu.cn

of modes and other experimental parameters. The results show that the resolution of phase measurements is increased to nearly twice compared to traditional double-path interferometers.

The remainder of this manuscript is organized as follows. In Sec. II, we introduce general procedures of a double-path multi-mode interferometer and give a brief theoretical analysis of the spatial interference. In Sec. III, we describe our experiment setup and demonstrate the spatial interference pattern experimentally. The dependence of the time domain fringes on number of modes and other experimental parameters are demonstrated both theoretically and experimentally in Sec. IV. Then we discuss the robustness of the measurements in Sec. V and give a conclusion in Sec. VI.

II. PRINCIPLES OF DOUBLE-PATH MULTI-MODE INTERFEROMETER

A. Procedures of double-path multi-mode interferometer

The essential components and procedures of a double-path multi-mode interferometer are shown in Fig. 1. The whole procedure can be divided into three steps. *Step 1 (S1): Create a double-path configuration.* A BEC on single magnetic sub-level $|F, m_F\rangle$ is prepared in a harmonic trap as the initial state [Fig. 1(a)], where F and m_F are the hyperfine structure quantum number and magnetic quantum number, respectively. Through a Majorana transition, the internal state of the atoms are transferred into a superposition state of two magnetic sub-levels $|F, m_F^{(I)}\rangle$ and $|F, m_F^{(II)}\rangle$ with equal coefficients (we denote these sub-levels as $|I\rangle$ and $|II\rangle$ and leave out the hyperfine quantum number F for convenience in the following discussions). The double-path configuration is achieved by coupling external states (i.e., positions and momenta) and internal states together [Fig. 1(b)] through a gradient magnetic field which lasts for T_d (I and II also denote the two paths in the following). *Step 2 (S2): Generate a multi-mode structure.* A radiofrequency (RF) pulse is implemented to further separate each state $|I\rangle$ ($|II\rangle$) into $N = 2F + 1$ sub-levels, followed by an evolution of time T_N in a gradient magnetic field, constructing the multi-mode structure [Fig. 1(c)]. *Step 3 (S3): Interfere and observe.* Finally, during the time-of-flight (TOF), the atomic clouds expand and interfere with each other [Fig. 1(d)], before an absorption imaging is taken.

B. Analysis of the spatial interference

In this subsection, we analyze the spatial interference of the double-path multi-mode interferometer and give the wavefunction for each stage shown in Fig. 1. Each

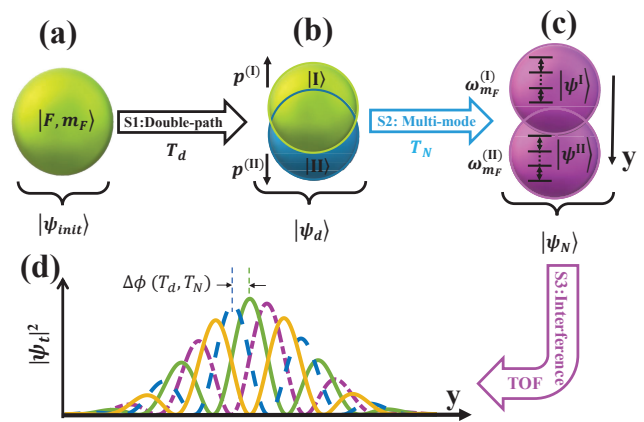


FIG. 1. (Color online) The schematic of double-path multi-mode interferometer. An initial BEC in (a) is converted to two coherent wavepackets served as paths $|I\rangle$ and $|II\rangle$ in (b) (whose momenta are $p^{(I)}$ and $p^{(II)}$ respectively) through a Majorana transition and an evolution of time T_d in the gradient magnetic field, which we refer to as the Step 1 (S1), or the double-path operation. In our Step 2, each wavepacket is converted to a superposition of several Zeeman sub-levels by a RF pulse. After the evolution in the gradient magnetic field with different phase evolution rate $\omega_{m_F}^{(I,II)}$ during time T_N , we got the superposition states in (c). Finally, after the time-of-flight (TOF) we observe the interference (d) of two superposition states by absorption imaging, where $\Delta\phi(T_d, T_N)$ is the relative phase between adjacent mode fringes.

state can be expressed as a direct-product of internal state, which takes into account the multi-mode effect and external states.

(a) *Initial state* $|\psi_{init}\rangle$ [Fig. 1(a)]. The initial BEC can be denoted as $|\psi_{init}\rangle = |F, m_F\rangle |p_0, y_0\rangle$ (we confine our description of external states to y -direction for simplicity).

(b) *Double-path state* $|\psi_d\rangle$ [Fig. 1(b)]. After the double-path operation T_d , the state becomes

$$|\psi_d\rangle = \frac{1}{\sqrt{2}} \sum_{j=I,II} e^{-i\xi^{(j)}} |j\rangle |p^{(j)}, y^{(j)}\rangle \quad (1)$$

Here, the phases $\xi^{(I,II)}$ are due to the state-dependent (and thus path-dependent) evolution. In magnetic field, the phase evolution rate of each state is determined by its local energy, which is a sum of the kinetic energy and the Zeeman-split energy[30, 32]. Therefore, the momentum, the magnetic sub-level and the local amplitude of the magnetic field together determined the phase evolution rate.

(c) *Double-path multi-mode state* $|\psi_N\rangle$ [Fig. 1(c)]. In the next step to implement multi-mode, both $|I\rangle$ and $|II\rangle$ are further separated into N sub-levels by the RF pulse respectively. After the second phase evolution T_N in two

paths, the state becomes

$$|\psi_N\rangle = \frac{1}{\sqrt{2}} \sum_{j=I,II} \sum_{m_F} b_{m_F}^{(j)} |m_F\rangle e^{-i[\theta_{m_F}^{(j)} + \varphi_{m_F}^{(j)}]} |p^{(j)}, y^{(j)}\rangle \quad (2)$$

where $\theta_{m_F}^{(I,II)}$ is the initial phase from the RF pulse, $\varphi_{m_F}^{(I,II)}$ takes into consideration the phases accumulated during the time T_N in both paths. To observe interference pattern, it is necessary that the final relative velocity between the two interfering wave packets is much smaller than the expansion velocity of each one of them, so that the interfering wave packets are well-overlapped [32].

(d) *Observed interfering state* $|\psi_t\rangle$ [Fig. 1(d)]. Finally, after TOF, the final state $|\psi_t\rangle$ can be re-expressed as

$$|\psi_t\rangle = \frac{1}{\sqrt{2}} \sum_{j=I,II} e^{-i\varphi_r^{(j)}} |\psi^{(j)}\rangle |p^{(j)}, y^{(j)}\rangle \quad (3)$$

where $e^{-i\varphi_r^{(I,II)}}$ are the overall phases of the two wavepackets, and $|\psi^{(I,II)}\rangle = \sum_{m_F} b_{m_F}^{(I,II)} e^{-i\phi_{m_F}^{(I,II)}} |m_F\rangle$ are the wavefunctions for the two superposition states, in which $\phi_{m_F}^{(I,II)} = \theta_{m_F}^{(I,II)} + \varphi_{m_F}^{(I,II)} - \varphi_r^{(I,II)}$.

The interference pattern is described by the atomic density distribution

$$\rho(y) = \langle \psi_t | \psi_t \rangle = 1 + V_N(T_d, T_N) \cos(\kappa y + \eta) \quad (4)$$

where $\kappa = (p^{(II)} - p^{(I)})/\hbar$ is the spatial frequency of the fringes, $\eta = \varphi_r^{(II)} - \varphi_r^{(I)}$ is the overall phase of the interference fringes. $V_N(T_d, T_N) = |\langle \psi^{(I)} | \psi^{(II)} \rangle|$ is the visibility of the interference fringes, which is influenced by different relative phase evolution between the same internal modes in the two paths.

Here the relative phase is accumulated in two ways here. First, an overall phase of each of the two paths (or the wavepackets in the two paths) is obtained, which is mainly determined by the duration T_d of the gradient magnetic field. This overall relative phase determines the profile of the interference pattern. Second, the relative phases between different states within one path (wavepacket) emerge during T_N and the TOF, which can be characterized by the state-dependent phase evolution rate $\omega_{m_F}^{(I,II)}$. We address our attention on the visibility, which shows a periodic dependence on T_N , which forms the so-called time domain interference. A remarkable feature of the multi-mode interferometer is the enhancement of resolution, which is defined as (fringe-period)/(full-width-half-maximum), through the increase in internal modes. Note that so far we haven't taken the shape of the wavepackets into consideration and give the formula for V_N . The wavepacket function and the dependence of visibility on T_N and T_d will be discussed in detail in Sec. IV.

III. EXPERIMENTAL DEMONSTRATION OF THE INTERFEROMETER

We prepare a BEC of ^{87}Rb with typically 1.0×10^5 atoms in the $|F=2, m_F=2\rangle$ state as our initial state, which is confined in a magnetic and optical hybrid harmonic trap with the trap frequencies $(\omega_x, \omega_y, \omega_z) = 2\pi \times (28 \text{ Hz}, 55 \text{ Hz}, 65 \text{ Hz})$. The preparation of the BEC is similar to our previous experiments[33, 34]. The magnetic sub-levels are considered as modes in the interferometer, with different phase evolution rate in magnetic field. Therefore, the hyperfine state number F has determined our maximum number of modes $N_{\text{max}} = 5$ ($m_F = -2, \dots, 2$). Our initial BEC temperature $\simeq 50 \text{ nK}$ guarantees the coherence of the atomic wavepackets. The atoms experience a magnetic field with amplitude of hundreds of milligauss, which resulted in a Zeeman split of $\simeq 310 \text{ kHz}$, and gradient of $\partial_y B = 12.4 \text{ G/cm}$.

In the double-path operation, we choose magnetic sub-levels $|F=2, m_F=1, 2\rangle$ as the states $|I, II\rangle$, which can be achieved by a non-adiabatic Majorana transition. Here the fine tunable spin projection of the non-adiabatic Majorana transition is achieved by precisely modulating the rotation of the magnetic field, where the transition time is chosen as $15.0 \mu\text{s}$ [31]. It transfers the initial state into $|m_F=2\rangle$ and $|m_F=1\rangle$ almost equally, leaving other states negligible, which is better than RF as a one-to-two beam splitter[31]. However, in the multi-mode operation, RF pulse behaves more effectively to divide both the two wavepackets ($|I\rangle$ and $|II\rangle$) into five states as evenly as possible[16]. So we choose RF in the multi-mode operation and set the duration of the RF pulse as $\tau_R = 10.0 \mu\text{s}$, whose frequency is set to the resonant frequency 310 kHz to match the Zeeman split. The pulse amplitude is a selected constant in order to achieve a one-to-five beam splitter, which makes both $|I\rangle$ and $|II\rangle$ transferred into all five Zeeman states.

The observed fringes are actually a superposition of the interference fringes of different modes. And the visibility depends on the relative phase between the interference fringes of different modes $|m_F\rangle$, where the fringe of each mode is formed by the same mode in the two paths. The relative phase can be investigated by tuning T_d and T_N . When all the modes are totally in phase, the visibility could reach $V_N = 1.0$ in theory. Setting $T_d = 8.0 \mu\text{s}$ and $T_N = 133.0 \mu\text{s}$, we observed the clearest interference, as shown in Fig. 2(a1). If the modes are partially in phase, the visibility drops but remains a non-zero value [Fig. 2(a2)], in which $T_d = 18.0 \mu\text{s}$ and $T_N = 146.0 \mu\text{s}$. And when all the fringes are complementary in space, the pattern without fringes is observed as shown in Fig. 2(a3), where $T_d = 28.0 \mu\text{s}$, and $T_N = 146.0 \mu\text{s}$. All of the images in this paper are taken by absorption imaging after TOF 26 ms.

To take into account the shape of the atomic cloud and the imperfection in the overlap between wavepackets of the two paths, we model the atomic clouds as the sum of

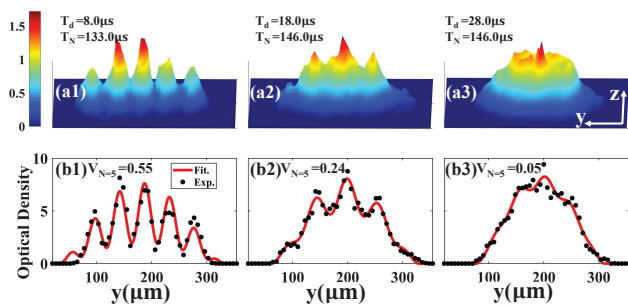


FIG. 2. (Color online) (a1)-(a3) show the single-shot spatial interference pattern with $N = 5$ interference modes after $T_{TOF} = 26$ ms, in which (a1) $T_d = 8.0 \mu\text{s}$, $T_N = 133.0 \mu\text{s}$, (a2) $T_d = 18.0 \mu\text{s}$, $T_N = 146.0 \mu\text{s}$ and (a3) $T_d = 28.0 \mu\text{s}$, $T_N = 146.0 \mu\text{s}$, with different relative phase between adjacent modes. (b1)-(b3) show the data (black points) in (a1)-(a3) integrated along the z direction and fit the data by Eq. (5) (red solid lines) and the visibilities are 0.55, 0.24 and 0.05, respectively.

two Thomas-Fermi wavepackets[32]

$$\Lambda = \rho \sum_{j=I,II} F^{(j)}(y) \quad (5)$$

Here $F^{(j)}(y) = A^{(j)} \max \left\{ \left[1 - (y - y_0^{(j)})^2 / 2(\sigma^{(j)})^2 \right]^{3/2}, 0 \right\}$ is the Thomas-Fermi function, $A^{(j)}$ is the amplitude, $y_0^{(j)}$ represents the center of the atomic cloud and $\sigma^{(j)}$ is the width of the wavepacket. We integrate the data in Fig. 2(a1) along the z -axis and fit it by Eq. (5), which shows a higher visibility $V_{N=5} = 0.55$ with a fringe spacing of $\lambda = 2\pi/\kappa = 46 \mu\text{m}$, as shown in Fig. 2(b1). However, the visibility reduces to $V_{N=5} = 0.24$ [Fig. 2(b2)] and $V_{N=5} = 0.05$ [Fig. 2(b3)] with other values of T_d and T_N . This means the relative phase can influence the visibility and we will discuss it in the following sections.

IV. THE RESOLUTION OF TIME DOMAIN INTERFERENCE

A. Formulating the time domain interference

The most important difference between a double-path multi-mode interferometer and a traditional double-path interferometer lies on that the visibility is modulated by the phase difference between two paths, and thus the visibility exhibits a periodic change and cause the emergence of the so-called time domain interference. The peak widths in time domain fringes is determined by number of modes N as well as the initial relative phase between the same mode in two paths $\Delta\theta_{m_F}$. Now in this section, following Eq. (4) in Sec. II B, we derive the formula for the visibility $V_N(T_d, T_N)$ and discuss its dependence on T_d and T_N .

The visibility of the spatial interference fringes is[35]

$$\begin{aligned} V_N(T_d, T_N) &= \left| \langle \psi^{(I)} | \psi^{(II)} \rangle \right| \\ &= \left| \sum_{m_F=3-N}^2 b_{m_F}^{(II)} b_{m_F}^{(I)} e^{-i[\phi_{m_F}^{(I)} - \phi_{m_F}^{(II)}]} \right| \\ &= \left| \sum_{m_F=3-N}^2 b_{m_F}^{(II)} b_{m_F}^{(I)} e^{-i\Delta\phi_{m_F}} \right| \end{aligned} \quad (6)$$

where $N = 3, 4, 5$ is the number of the modes. When considering the phase evolution, only the relative phase is relevant. Therefore, we use the $|m_F = 2\rangle$ state as a reference and denote the phase of each component as $\phi_{m_F}^{(j)} = \varphi_{2 \leftarrow m_F}^{(j)} + \theta_{m_F}^{(j)}$ and $\varphi_{2 \leftarrow m_F}^{(j)} = \varphi_{m_F}^{(j)} - \varphi_2^{(j)} = (2 - m_F)\omega^{(j)}T_N$, where $\omega^{(j)}$ is the relative phase evolution rate between adjacent modes in path j . The relative phase evolution rate between the two paths is defined as $\Delta\omega = \omega^{(I)} - \omega^{(II)}$, where $\omega^{(I)}$ and $\omega^{(II)}$ are the phase evolution rates in each path, respectively. The relative phase of the $|m_F\rangle$ states in two paths is $\Delta\phi_{m_F} = \phi_{m_F}^{(I)} - \phi_{m_F}^{(II)} = (2 - m_F)\Delta\omega T_N + \Delta\theta_{m_F}$, where the relative phase evolution rate $\Delta\omega$ is dependent on T_d , and $\Delta\theta_{m_F} = \theta_{m_F}^{(I)} - \theta_{m_F}^{(II)}$ is the initial relative phase of the $|m_F\rangle$ modes in the two superposition states. The relative phase between two adjacent components is

$$\begin{aligned} \Delta\phi &= (\Delta\phi_{m_F} - \Delta\theta_{m_F}) - (\Delta\phi_{m_F-1} - \Delta\theta_{m_F-1}) \\ &= \Delta\omega T_N \end{aligned} \quad (7)$$

From Eq. (7) we know that the relative phase $\Delta\phi$ (and thus the visibility V_N) is periodically modulated with the period $2\pi/\Delta\omega$, leading to the time domain fringes. Combining the time domain fringes with the spatial interference fringes we discussed above, our double-path multi-mode interferometer can be considered as a space-time interferometer. So far, we can see that the time domain fringes are influenced by number of modes, the initial relative phase and the relative phase evolution rate between two paths $\Delta\omega$, which will be discussed with experiments in the following subsections.

B. Sharper time domain fringes with more modes

We experimentally study how the structure of the time domain fringes change with the number of modes N , as shown in Fig. 3. Different modes N are achieved by changing the power of the RF, while the RF duration is unchanged. T_d is chosen as $42.5 \mu\text{s}$ to maximize the visibility (see Appendix. A). In Fig. 3(a), compared to the time domain fringes of two-path two-mode interference (solid black line), the time domain fringes of the double-path three-mode visibility represents two peaks in one period. According to Figs. 3(b) and 3(c), more complex internal structure of the time domain fringes emerges, in which more peaks appear in each cycle and

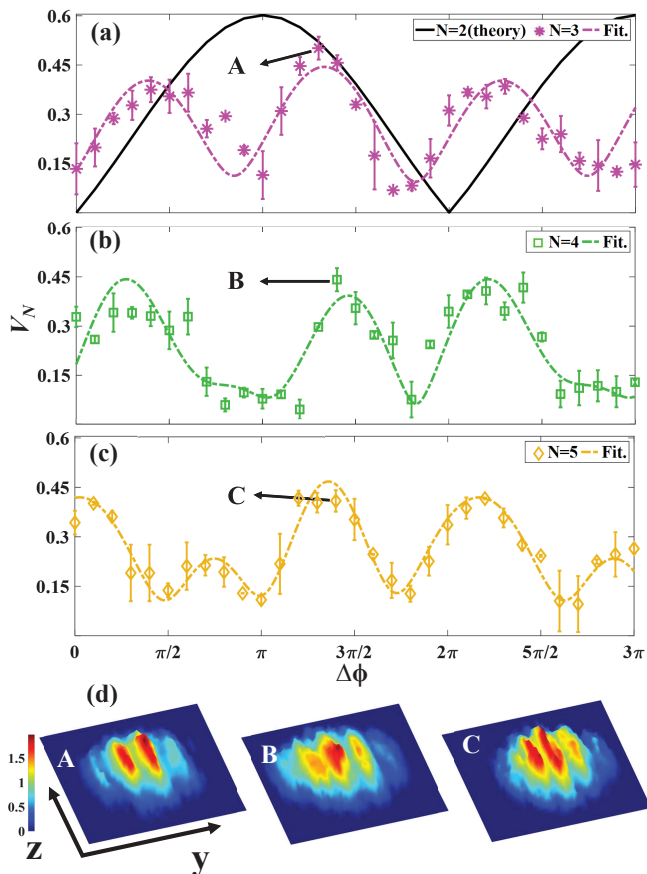


FIG. 3. (Color online) The oscillation of visibility V_N with $\Delta\phi$ with (a) $N = 3$ modes, (b) $N = 4$ modes and (c) $N = 5$ modes, with $T_d = 42.5 \mu\text{s}$. The points and the dashed lines show the experimental data and fit respectively. Each data point is a statistical average of four repeated experiments and the error bar shows the standard deviation. The theoretical result of a two-mode situation is shown by the black solid line in (a) for comparison. We set the phase to be zero at $T_N = 110.0 \mu\text{s}$ as a reference and the data is measured from $T_N = 110.0 \mu\text{s}$ to $T_N = 140.0 \mu\text{s}$. $\Delta\omega = 0.31(3) \text{ rad}/\mu\text{s}$ is used in all three measurements. (d) The TOF image near the main peak with different number of modes N . The image in A, B and C correspond to points A, B and C in (a), (b) and (c), respectively.

the fringes become sharper. This comes from two mechanisms: high-order harmonics induced by multi-modes and the influence of different initial relative phase, which will be discussed in detail in next subsection.

By fitting the data with Eq. (6), we find the periods of the time domain fringes for different N are almost the same, and $\Delta\omega$ is measured as $0.31(3) \text{ rad}/\mu\text{s}$ in Fig. 3, which nearly matches the theoretical estimation $\Delta\omega_{est} = 0.27(3) \text{ rad}/\mu\text{s}$. Meanwhile, as the number of modes increases from Fig. 3(a) to 3(b), the visibility of the main peak (A, B, C) remains essentially unchanged around 0.45, where the corresponding TOF images are shown in Fig. 3(d) respectively. We get the

full-width-half-maximum of the main peaks and then the corresponding resolution are measured as (a) 2.4(3), (b) 2.7(3) and (c) 3.0(3). They are all larger than the resolution of an ideal double-path two-mode interferometer 1.5. The deviation of the visibility from ideal value is due to the contribution of the residual magnetic field fluctuations, which is estimated as 1 mG, and time control accuracy (see Appendix. B). So with Fig. 3, we demonstrate that as the number of modes increases, the main peak visibility of the fringes of the time domain interference is basically unchanged, and the phase resolution is gradually improved.

C. Higher resolution with appropriate initial phase

It is necessary to point out that the initial phase of each mode could influence the shape of time domain fringes. In order to give a general discussion, we don't confine ourselves to five-mode situation and consider arbitrary number of modes. The wave function of a multi-mode superposition state can be defined as[30]

$$|\psi^{(j)}\rangle = \zeta(y) \sum_{l=1}^N e^{-i(\omega_l^{(j)} T_N + \theta_l^{(j)})} |l\rangle \quad (8)$$

which $j = I, II$ represents the two paths, $\zeta(y) = \frac{\chi(y)}{\sqrt{2N}} e^{-ik^{(j)}y}$ is represents a moving wavepacket, $\chi(y)$ is a (one-dimensional) localized, normalized wave function, $k^{(j)}$ is the wave vector of the j -th wave packet. Here, the notion l corresponds to the magnetic sub-levels $|m_F\rangle$ used in previous discussions. $\omega_l^{(j)} = l\omega^{(j)}$ represents the phase evolution rate of the l -th mode ($|l\rangle$ state) in path j . When the two wavepackets are fully overlapped, the density distribution is given by $|\psi^{(I)}\rangle + |\psi^{(II)}\rangle^2$, leading to the visibility

$$V_N = \left| \sum_{l=1}^N \frac{1}{N} e^{-i(l\Delta\phi + \Delta\theta_l)} \right| \quad (9)$$

where $\Delta\phi = \Delta\omega T_N$ is the relative phase of the fringes between adjacent modes and $\Delta\omega$ is relative phase evolution rate. The $\Delta\theta_l = \theta_l^{(I)} - \theta_l^{(II)}$ is the initial relative phase of the $|l\rangle$ state in two wavepackets.

The sharpness of the peaks (and thus the resolution) varies for different $\Delta\theta_l$. Fig. 4(a) is under the condition that the phases $\Delta\theta_l$ are all the same for any l . In that case, if we denote $\Delta\omega T_N = 2n\pi/N$, then when n is a non-negative integer but isn't the multiple of N , the visibility $V_N = 0$, while the visibility achieves $V_N = 1$ when n is the multiple of N and a major peak is observed in this case. As a result, the peak of the visibility gets much sharper as N increases, which leads to a higher resolution. It is the harmonics that cause the peak width to decrease with the number of modes increasing in this case [10]. A remarkable feature of our interferometer is that the

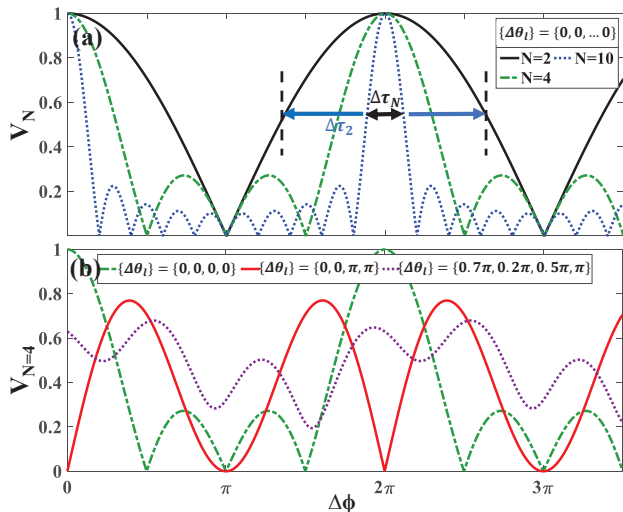


FIG. 4. (Color online) The dependence of visibility on number of modes N and initial relative phase of the same mode in two paths $\Delta\theta_l$. (a) shows the dependence on N in a situation that the relative initial phase $\Delta\theta_l$ are all zero. The full-width-half-maximum (FWHM) $\Delta\tau_N$ of the N -mode fringe is $2/N$ times of that of the 2-mode fringe. (b) shows the dependence on $\Delta\theta_l$ using $N = 4$ as an example. The green dashed line, red solid line and purple dotted line show the fringes with $\{\Delta\theta_l\} = \{\Delta\theta_1, \Delta\theta_2, \Delta\theta_3, \Delta\theta_4\} = \{0, 0, 0, 0\}$, $\{\Delta\theta_l\} = \{0, 0, \pi, \pi\}$ and $\{\Delta\theta_l\} = \{0.7\pi, 0.2\pi, 0.5\pi, \pi\}$, respectively.

enhancement of resolution with $N/2$ times is achieved without reduction in visibility.

However, if the initial relative phase of each state $\Delta\theta_l$ varies from mode to mode [Fig. 4(b) serves as an example at $N = 4$], the visibility could reach neither the maximum $V_N = 1.0$ nor the minimum $V_N = 0$. Instead, the time domain fringe shows more than one main peaks in one period. For some specific configurations for special initial relative phase is chosen, for example, $\{\Delta\theta_l\} = \{\Delta\theta_1, \Delta\theta_2, \Delta\theta_3, \Delta\theta_4\} = \{0, 0, \pi, \pi\}$, the interference fringes with two main peaks in each period are observed, as shown by the red solid line in Fig. 4(b). Therefore, the resolution deteriorates more or less, which explains what we observed in Fig. 3. Meanwhile, if the initial relative phase is chosen randomly as, e.g., $\{\Delta\theta_l\} = \{0.7\pi, 0.2\pi, 0.5\pi, \pi\}$, there are no the interference fringes with obvious periodic characteristics. Therefore, the initial phase $\Delta\theta_l$ needs to be well controlled to achieve the highest possible visibility and clear interference fringe in time domain.

D. Investigating relative phase evolution rate $\Delta\omega$

When one studies the traditional double-path interference, the difference of the phase evolution rates between the two paths results in a change in the period of the spatial interference fringes. When considering a double-path multi-mode interference in the time domain, however, we

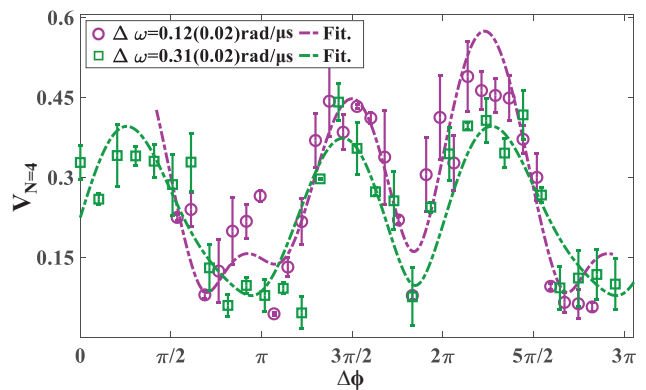


FIG. 5. (Color online) The oscillation of visibility with $\Delta\phi$ under the conditions of different $\Delta\omega$ at $N = 4$. Dashed lines show the fit results. The green (purple) points represent for $T_d = 42.5 \mu\text{s}$ ($T_d = 17.0 \mu\text{s}$) and corresponding $\Delta\omega = 0.31(2) \text{ rad}/\mu\text{s}$ ($\Delta\omega = 0.12(2) \text{ rad}/\mu\text{s}$). Each data point is a statistical average of four repeated experiments and the error bar shows the standard deviation. We set the phase of the green line at $T_N = 110.0 \mu\text{s}$ to be zero as a reference, and the data is measured from $110.0 \mu\text{s}$ to $140.0 \mu\text{s}$. For purple points we set the valley phase to be the same as the valley value of the green line around 2π and the data is measured from $100.0 \mu\text{s}$ to $166.0 \mu\text{s}$.

address our attention to how the difference between two paths influences the period of the time domain fringe, which corresponds to $2\pi/\Delta\omega$. $\Delta\omega$ is mainly affected by T_d , i.e., the double-path operation, since the path difference lies in the difference between the momenta of the two wavepackets and their positions in the harmonic trap.

To show the effects of $\Delta\omega$, we measured the time domain fringes for different T_d for number of modes $N = 4$, as shown in Fig. 5. The purple and green lines are obtained with $\Delta\omega = 0.12(2) \text{ rad}/\mu\text{s}$ ($T_d = 17.0 \mu\text{s}$) and with $\Delta\omega = 0.31(2) \text{ rad}/\mu\text{s}$ ($T_d = 42.5 \mu\text{s}$), respectively. The resolution is measured as $2.7(3)$ and, the purple and green lines show a similar period with respect to phase $\Delta\omega T_N$, so the period $2\pi/\Delta\omega$ of the green line in time domain is lower than the half of the purple line with respect to time T_N . As a result, the resolution of the phase measurement of the green line is more than doubled compared to the purple line in time domain. In general, when increasing the difference of the two paths in the double-path multi-mode interferometer by increasing T_d , we can decrease the period of the time interference fringes $2\pi/\Delta\omega$ and improve the measurement resolution of the interference fringes in time domain.

V. COHERENCE ANALYSIS

In this section, we analyze the coherence of the fringes and the robustness of the measurements, and in particular, whether the fringes move and whether the visibility changes from shot to shot, in order to support that the

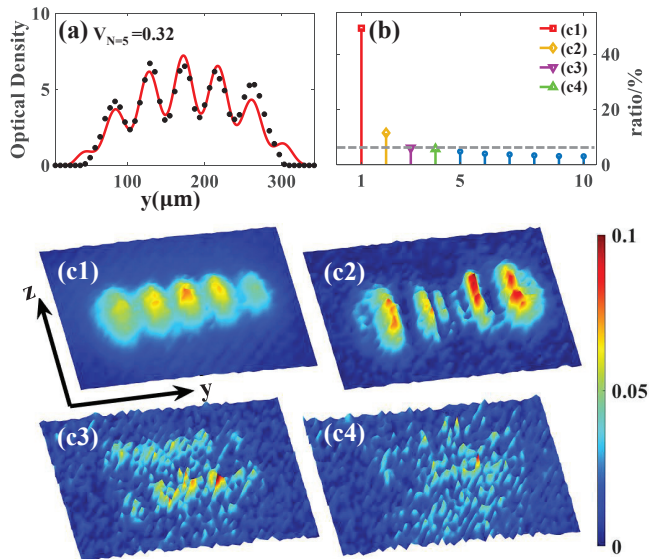


FIG. 6. (Color online) (a) Averaged interference fringes of 42 consecutive measurements. The black points are the experimental data integrated along the z direction, and the red line is the fitted curve by Eq. (5) and get the visibility 0.32. (b) The percentage ratio of the first ten principle components (PCs). The gray dashed line shows the level of background noise ($\simeq 5\%$) and indicates the threshold for distinguishing important PCs. PCs of interest are highlighted with different colors, which correspond to (c1)-(c4) from left to right. Note that the first four PCs are significantly reduced as the order of PC increases. (c1) represents the average of interference fringes. (c2) and (c3) correspond to spatial fluctuations along y - and z -axes, respectively. They together represent atom cloud position fluctuations in the y - z plane. (c4) represents noise sources from imaging light.

interference is robust. We take the situation shown in Fig. 2(a1) as an example, where 42 consecutive experiment data sets were taken under identical conditions. The visibility of the average reduces to $V_{N=5} = 0.32$ as shown in Fig. 6(a) from the single-shot visibility $V_{N=5} = 0.55$ as shown in Fig. 2(a). That we can still observe clear fringes in the averaged image indicates that the relative phase $\Delta\phi$ is quite stable, and we attribute the decrease of visibility from single-shot to average to the noises in experiments.

In order to understand the contribution of different noise sources, following our previous work Ref. [36, 37], we perform a principle component analysis (PCA) on the data sets. Fig. 6(b) shows percentages of the total variance associated with the first 10 PCs. We find that the components of higher than the fourth order are negligible because they're below the level of background noise $\simeq 5\%$. We reconstruct the contribution of the first four principle components (PCs), which are shown in Figs. 6(c1)-6(c4). Fig. 6(c1) exhibits the main features of the original experimental image. The second and the third PCs shown in Figs. 6(c2)-6(c3), whose percentages

are of the same order of magnitude, reflect the position uncertainty of the fringes along y -axis and z -axis, respectively. They together represent the position fluctuations of the atomic clouds position in y - z plane. The noises make the position fluctuations slightly anisotropic due to different eigenvalues. They come from the system noises such as the electrical noises of the RF coupling circuit and magnetic field control circuit, as well as the fluctuations of the gradient magnetic field $\partial_y B$. The fluctuations in the atomic region of Fig. 6(c4) is comparable to the background noise, which could be attributed to the photon shot noise and CCD camera dark current noise.

VI. CONCLUSION

We demonstrated the principles of a double-path multi-mode matter wave interferometer, which is different from traditional double-path interference with single component in each path. One can observe not only spatial interference fringes, but also time domain interference of the visibility. Meanwhile, we experimentally demonstrated its performance with number of modes being three, four and five. The period of time domain fringes is independent to the modes number. However, a remarkable feature of the double-path multi-mode interferometer is the enhancement of phase measurement resolution in time domain with the increasing of the modes number, where the double-path five-mode interferometer is enhanced twice compared to an ideal double-path two-mode interferometer [Fig. 3(c)]. Last but not least, the relative phase evolution rate $\Delta\omega$ can be controlled by adjusting the difference between the two paths accumulated in the T_d stage. Furthermore, the interferometer was implemented in a trap with a weak magnetic field, making it easy to be integrated into a miniaturized interferometer on an atomic chip and convenient to be combined with optical lattice during the process of the phase evolution.

ACKNOWLEDGMENTS

We thank Weidong Li, Baoguo Yang, Peng Zhang, Xinhao Zou and Xiaopeng Li for helpful discussion. This work is supported by the National Basic Research Program of China (2016YFA0301501) and the National Natural Science Foundation of China (61727819, 11934002, 91736208).

Appendix A: Choosing appropriate T_d for clear time domain fringe

In the main text, we mainly discuss how the visibility is affected by T_N . In fact, T_d also has an impact on visibility. The role of the T_d is mainly reflected in two aspects: modify initial phase $\Delta\theta_{m_F}$ and affect the quality

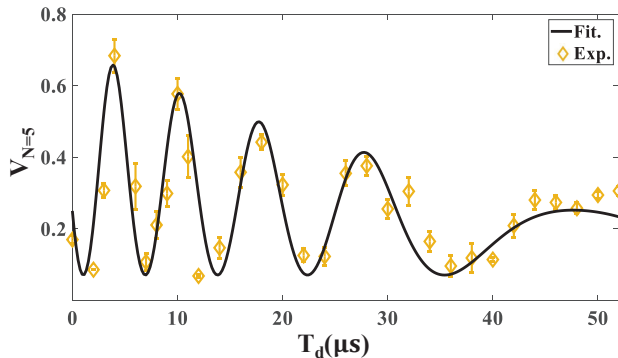


FIG. 7. (Color online) The visibility V_N versus T_d when $T_N = 146.0 \mu\text{s}$ and $N = 5$. The yellow points are the experimental data with average of three shots, and the black solid line is obtained by fitting the curve using Eq. (A1).

of the overlapping between two wavepackets. By choosing appropriate T_d , we can get a high maximum visibility time domain fringes.

In order to demonstrate the effect of T_d , we keep $T_N = 146.0 \mu\text{s}$ unchanged, and measure the dependence of visibility on T_d , as shown in Fig. 7. It shows a clear trend that the visibility experiences an damping oscillation as T_d increases. To count for this phenomenon, we model this process using the following empirical formula Eq. (A1) to fit the experimental data.

$$V_N = R \exp(-\gamma T_d) [1 + \cos(\omega_d - \varepsilon T_d) T_d + \alpha] + \beta \quad (\text{A1})$$

where R is the amplitude, γ is the damping factor. The phase evolution rate is modeled in a gradual changing way $\omega_d - \varepsilon T_d$, where εT_d represents for a linear change. α represents the initial phase of the time domain fringes and β is a bias. The oscillation amplitude gradually reduces, because the wave packet overlap of the two paths becomes smaller.

When a good set of initial phases $\Delta\theta_{m_F}$ is chosen, the interference fringes could reach a high maximum visibility, as demonstrated in Fig. 4(b). Therefore, we could obtain the appropriate set of $\Delta\theta_{m_F}$ by selecting T_d at the peak position in the curve in Fig. 7 to achieve a clear time domain interference fringe, which shows a high maximum visibility and a simple period. Considering that the frequency $\Delta\omega$ will be too small to measure in experiment if T_d is too small, the smallest value for T_d is chosen to be $17.0 \mu\text{s}$ as in Fig. 5. On the other hand, to guarantee that two wavepackets are sufficiently overlapped for high visibility, T_d should be chosen to less than $50.0 \mu\text{s}$. As result, the largest value for T_d is chosen as $42.5 \mu\text{s}$ as in Fig. 3.

Appendix B: Estimating $\Delta\omega$ from experiments

In order to estimate the relative phase evolution rate $\Delta\omega$ between two paths, we analyze the phase evolution of

each Zeeman sub-level based on experimental parameters such as T_d and T_N . After the double-path evolution T_d and the multi-mode evolution T_N in the harmonic trap and the TOF with the expansion time T_{TOF} , the phase of each state $|m_F\rangle$ in path $j = I, II$ can be expressed as $\varphi_{m_F}^{(j)} = (m/2\hbar T_{TOF}) y_{m_F}^{(j)2} + m v_{m_F}^{(j)} y_{m_F}^{(j)} / \hbar$ [5, 6, 38] (here we ignore the initial phase $\theta_{m_F}^{(j)}$, which is independent of $\Delta\omega$), where m is the atomic mass, \hbar is reduced Planck constant, $y_{m_F}^{(j)}$ is the position of the atomic cloud in $|m_F\rangle$ state of the j path after the TOF, $v_{m_F}^{(j)}$ is the velocity of the atomic cloud in $|F, m_F^{(j)}\rangle$ state. Here the $|m_F = 2\rangle$ state is chosen as the phase reference, then we have $\phi_{m_F}^{(j)} = \varphi_{m_F}^{(j)} - \varphi_2^{(j)}$. We put $\phi_{m_F}^{(j)}$ into Eq. (7) and adopt $m_F = 2$, then we have

$$\Delta\phi = \frac{m}{\hbar T_{TOF}} \delta y_1 \delta y_{2\leftarrow 1}^{(j)} + \frac{m}{\hbar} \delta v_1 \delta y_{2\leftarrow 1}^{(j)} + \frac{m}{\hbar} \delta y_1 \delta v_{2\leftarrow 1}^{(j)} \quad (\text{B1})$$

where

$$\delta v_1 = v_1^{(I)} - v_1^{(II)} = a T_d \quad (\text{B2})$$

$$\delta v_{2\leftarrow 1}^{(j)} = v_1^{(j)} - v_2^{(j)} = a T_N \quad (\text{B3})$$

$$\delta y_1 = y_1^{(I)} - y_1^{(II)} \simeq a T_d T_{TOF} \quad (\text{B4})$$

$$\delta y_{2\leftarrow 1}^{(j)} = y_1^{(j)} - y_2^{(j)} \simeq a T_N T_{TOF} \quad (\text{B5})$$

Here δv_1 and δy_1 are the velocity difference and position difference after TOF between the atomic wave packets of the same mode ($m_F = 1$) in two paths. $\delta v_{2\leftarrow 1}^{(j)}$ and $\delta y_{2\leftarrow 1}^{(j)}$ are the velocity difference and position difference after TOF of the adjacent atomic wave packets in the same path, respectively. a is the acceleration between two adjacent modes in the trap, which is derived from the interaction between the adjacent states and the difference of gradient magnetic forces between them. We get $a \simeq 7.3 \text{ m/s}^2$ from experimental measurements in a duration of tens of microseconds[16].

Then, by substituting Eqs. (B2)-(B5) into Eq. (B1), we have the relative phase of adjacent component fringes

$$\Delta\phi \simeq 3 \frac{m}{\hbar} a^2 T_d T_{TOF} T_N = \Delta\omega T_N \quad (\text{B6})$$

where $\Delta\omega = 3 \frac{m}{\hbar} a^2 T_d T_{TOF}$ is relative phase evolution rate. After considering the systematic error, we have

$$\Delta\omega \simeq 3 \frac{m}{\hbar} a \delta y_1 \left[1 \pm \left(\frac{2\Delta a}{a} + \frac{\Delta T_d}{T_d} \right) \right] \quad (\text{B7})$$

Here $\Delta a = 0.3 \text{ m/s}^2$ comes from the position uncertainty of the wavepackets when measuring the acceleration a by 26 ms TOF image. $\delta y_1 = a T_d T_{TOF}$ is the distance of the two wavepackets after TOF and $\Delta T_d \simeq 100 \text{ ns}$ is the uncertainty of T_d . Meanwhile, considering that the gradient magnetic field keeps on during the RF duration ($\tau_R = 10.0 \mu\text{s}$), we actually estimate $\Delta\omega$ with $T_d + \tau_R/2$ instead of T_d , where $\tau_R/2$ is a compensation time.

-
- [1] A. D. Cronin, J. Schmiedmayer, and D. E. Pritchard, *Rev. Mod. Phys.* **81**, 1051 (2009).
- [2] D. M. Stamper-Kurn and M. Ueda, *Rev. Mod. Phys.* **85**, 1191 (2013).
- [3] H. H. Muntinga, H. Ahlers, M. Krutzik, A. Wenzlawski, S. Arnold, D. Becker, K. Bongs, H. Dittus, H. Duncker, N. Gaaloul, et al., *Phys. Rev. Lett.* **110**, 093602 (2013).
- [4] P. Lombardi, F. Schaefer, I. Herrera, S. Cherukattil, J. Petrovic, C. Lovecchio, F. Marin, and F. Cataliotti, *Opt. Express* **22**, 19141 (2014).
- [5] F. Dalfovo, S. Giorgini, L. P. Pitaevskii, and S. Stringari, *Rev. Mod. Phys.* **71**, 463 (1999).
- [6] J. Simsarian, J. Denschlag, M. Edwards, C. W. Clark, L. Deng, E. W. Hagley, K. Helmerson, S. Rolston, and W. D. Phillips, *Phys. Rev. Lett.* **85**, 2040 (2000).
- [7] M. H. Wheeler, K. M. Mertes, J. D. Erwin, and D. S. Hall, *Phys. Rev. Lett.* **93**, 170402 (2004).
- [8] S. Dimopoulos, P. W. Graham, J. M. Hogan, and M. A. Kasevich, *Phys. Rev. Lett.* **98**, 111102 (2007).
- [9] J. Grond, U. Hohenester, I. Mazets, and J. Schmiedmayer, *New J. Phys.* **12**, 065036 (2010).
- [10] I. Pikovski, M. Zych, F. Costa, and Č. Brukner, *New J. Phys.* **19**, 025011 (2017).
- [11] T. Schumm, S. Hofferberth, L. M. Andersson, S. Wildermuth, S. Groth, I. Bar-Joseph, J. Schmiedmayer, and P. Krüger, *Nat. Phys.* **1**, 57 (2005).
- [12] B. Yang, S. Jin, X. Dong, Z. Liu, L. Yin, and X. Zhou, *Phys. Rev. A* **94**, 043607 (2016).
- [13] D. Hu, L. Niu, S. Jin, X. Chen, G. Dong, J. Schmiedmayer, and X. Zhou, *Commun. Phys.* **1**, 29 (2018).
- [14] L. Pezzé and A. Smerzi, *Phys. Rev. Lett.* **102**, 100401 (2009).
- [15] B. Lücke, M. Scherer, J. Kruse, L. Pezzé, F. Deuretzbacher, P. Hyllus, O. Topic, J. Peise, W. Ertmer, J. Arlt, et al., *Science* **334**, 773 (2011), ISSN 0036-8075.
- [16] P. Tang, P. Peng, Z. Li, X. Chen, X. Li, and X. Zhou, *Phys. Rev. A* **100**, 013618 (2019).
- [17] G. Weihs, M. Reck, H. Weinfurter, and A. Zeilinger, *Opt. Lett.* **21**, 302 (1996).
- [18] M. Weitz, T. Heupel, and T. Hänsch, *Phys. Rev. Lett.* **77**, 2356 (1996).
- [19] M. W. Mitchell, J. S. Lundeen, and A. M. Steinberg, *Nature* **429**, 161 (2004).
- [20] J. Chwedeńczuk, F. Piazza, and A. Smerzi, *Phys. Rev. A* **87**, 033607 (2013).
- [21] T. Paul and T. Qureshi, *Phys. Rev. A* **95**, 042110 (2017).
- [22] M. Weitz, T. Heupel, and T. Hänsch, *Phys. Rev. Lett.* **77**, 2356 (1996).
- [23] J. Petrovic, I. Herrera, P. Lombardi, F. Schaefer, and F. S. Cataliotti, *New J. Phys.* **15**, 043002 (2013).
- [24] E. Andersson, T. Calarco, R. Folman, M. Andersson, B. Hessmo, and J. Schmiedmayer, *Phys. Rev. Lett.* **88**, 100401 (2002).
- [25] I. P. Magdalena Zych, Fabio Costa and Č. Brukner, *Nat. Commun.* **2**, 505 (2011).
- [26] J. J. Cooper, D. W. Hallwood, J. A. Dunningham, and J. Brand, *Phys. Rev. Lett.* **108**, 130402 (2012).
- [27] W. Li, T. He, and A. Smerzi, *Phys. Rev. Lett.* **113**, 023003 (2014).
- [28] J. Söderholm, G. Björk, B. Hessmo, and S. Inoue, *Phys. Rev. A* **67**, 053803 (2003).
- [29] J. Chwedeńczuk, *Phys. Rev. A* **96**, 032320 (2017).
- [30] Y. Margalit, Z. Zhou, S. Machluf, D. Rohrlich, Y. Japha, and R. Folman, *Science* **349**, 1205 (2015).
- [31] P.-J. Tang, P. Peng, X.-Y. Dong, X.-Z. Chen, and X.-J. Zhou, *Chin. Phys. Lett.* **36**, 050301 (2019).
- [32] S. Machluf, Y. Japha, and R. Folman, *Nat. Commun.* **4**, 2424 (2013).
- [33] L. Niu, S. Jin, X. Chen, X. Li, and X. Zhou, *Phys. Rev. Lett.* **121**, 265301 (2018).
- [34] S. Jin, X. Guo, P. Peng, X. Chen, X. Li, and X. Zhou, *New J. Phys.* **21**, 073015 (2019).
- [35] J. Schmiedmayer, C. R. Ekstrom, M. S. Chapman, T. D. Hammond, and D. E. Pritchard, *Journal de Physique II* **4**, 2029 (1994).
- [36] S. Cao, P. Tang, X. Guo, X. Chen, W. Zhang, and X. Zhou, *Opt. Express* **27**, 12710 (2019).
- [37] L. Niu, X. Guo, Y. Zhan, X. Chen, W. M. Liu, and X. Zhou, *Appl. Phys. Lett.* **113**, 144103 (2018).
- [38] C. Fort, P. Maddaloni, F. Minardi, M. Modugno, and M. Inguscio, *Opt. Lett.* **26**, 1039 (2001).